Effects of Thermal Annealing on Structural and Magnetic Properties of Lithium Ferrite Nanoparticles

Nataša G. Jović,*[,†] Ahmad S. Masadeh,[‡,§] Aleksandar S. Kremenović,[†,∥] Bratislav V. Antić,[†] Jovan L. Blanuša,[†] Nikola D. Cvjetičanin,[⊥] Gerardo F. Goya,[#] Marco Vittori Antisari,[▽] and Emil S. Božin[○]

Institute "Vinča", Laboratory of Theoretical and Condensed Matter Physics, P.O. Box 522, 11001 Belgrade, Serbia, Department of Physics and Astronomy, Michigan State University, East Lansing, Michigan 48824, Department of Physics, University of Jordan, Amman 11942, Jordan, Faculty of Mining and Geology, Laboratory for Crystallography, University of Belgrade, Đušina 7, 11000 Belgrade, Serbia, Faculty of Physical Chemistry, Studentski Trg 12-14, 11000 Belgrade, Serbia, Aragon Institute of Nanoscience & Condensed Matter Physics Department, University of Zaragoza, Zaragoza, Spain, ENEA, FIM Department, C.R. Casaccia, Via Anguillarese 301, 00060 Roma, Italy, Department of Applied Physics and Applied Mathematics, Columbia University, New York, New York 10027

Received: August 5, 2009; Revised Manuscript Received: October 12, 2009

Pure, crystalline, ∼10 nm lithium ferrite phase ($Li_{0.5}Fe_{2.5}O_4$), was successfully synthesized at very low temperature using a modified combustion method. The crystal structure and microstructure evolution of this system upon annealing were monitored by a careful investigation of X-ray diffractograms collected on a synchrotron source. Comparative analysis of the results obtained from the full profile Rietveld method (in reciprocal space) and the pair distribution function method (in direct space) was carried out. Nanocrystalline samples exhibit similar crystal structure, on average, with a partial ordering of Li^+ and Fe^{3+} ions between octahedral 4b and 12d sites on the spinel crystal lattice (space group $P4_332$). After annealing at 973 K, cation distribution changes to a completely ordered, resembling that which is seen in the bulk lithium ferrite. The PDF analysis reveals abnormally high values of oxygen atomic displacement parameters in tetrahedral 8c sites (O1) indicating a significant disordering of the O1 network and suggests migration of lithium ions from 4b sites to the outer layers of nanoparticles. Analysis of room temperature Mössbauer spectra has shown that the hyperfine field for Fe^{3+} ions in tetrahedral 8c sites is the most sensitive on increasing the particle size and improving the crystallinity. From the differential thermal analysis, it was found that a lower driving force is required to induce an order−disorder phase transition in nanocrysalline samples, compared to the bulk-like sample, presumably due to the higher crystal disordering in these samples.

1. Introduction

Lithium ferrite $Li_{0.5}Fe_{2.5}O_4$ spinel has been of great technological interest in many electromagnetic devices for a long time. High electrical resistivity, low eddy current losses, low magnetic losses, and very good thermal and chemical stability make lithium ferrite a material of great importance for microwave applications.[1] This soft ferrite material with high Curie temperature, square loop properties, and high saturation magnetization has also been used in ferrite-core memory systems. Thermal stability and safety of lithium ferrite make this material suitable for application in Li-ion batteries as a cathode material,[2] and recently as a potential gas sensor element.[3] Furthermore, due to the low fabrication cost, lithium ferrite has been increasingly used as a replacement for the more expensive yttrium iron garnet (YIG) in mass-scale microwave devices.

Bulk lithium ferrite is an inverse spinel that typically crystallizes in two polymorphic forms. The ordered α-phase (space group $P4_332$) is characterized by the presence of 1:3 ordering of Li^+ and Fe^{3+} ions on the octahedral sublattice in spinel structure, with corresponding cation distribution $(Fe^{3+})_{8c}[(Li^+_{0.5})_{4b}(Fe^{3+}_{1.5})_{12d}]$. The disordered β-phase (space group $Fd\bar{3}m$) possesses a random distribution of Li^+ and Fe^{3+} ions over the octahedral sites with cations distribution $(Fe^{3+})_{8a}[Li^+_{0.5}Fe^{3+}_{1.5}]_{16d}$. The order−disorder phase transition in bulk $Li_{0.5}Fe_{2.5}O_4$ occurs in the temperature range 1008−1028 K.[4]

In nanomaterials, the cation distribution can differ significantly from that in a bulk counterpart.[5] The large surface-to-volume ratio in nanoparticles has significant influence on their physical and chemical behavior. The atoms at the surface of the particles display an incomplete coordination shell which can result in ionic displacements, changes in the lattice parameters, and even provoke a nanoparticles' core/shell structure.[6,7]

In the study reported here, the pure nanocrystalline lithium ferrite phase has been successfully synthesized at very low temperature using the citrate gel precursor method. The study has been focused on the following issues: (i) the synthesis route, (ii) the evolution of the crystal structure and microstructure with changing annealing conditions, observed by X-ray powder diffraction and differential thermal analysis (DTA) methods, (iii)

* Corresponding author. Phone: +381 11 80 65 828. Fax: +381 11 80 65 829. E-mail: natasaj@vinca.rs.
† Institute "Vinča".
‡ Michigan State University.
§ University of Jordan.
∥ University of Belgrade.
⊥ Faculty of Physical Chemistry.
University of Zaragoza.
▽ ENEA.
○ Columbia University.

10.1021/jp907559y CCC: $40.75
Published on Web 11/09/2009

the comparative analysis of crystal structure and microstructural parameters obtained using Rietveld profile method and the atomic pair distribution function (PDF) approach, and (iv) changes of the Mössbauer parameters with increasing annealing temperature (i.e., crystallite size).

2. Experimental Section

2.1. Synthesis Procedure. A series of nanocrystalline lithium ferrite samples, $Li_{0.5}Fe_{2.5}O_4$, was synthesized by a modified combustion method using citric acid as a fuel for combustion reaction. Lithium nitrate and iron(III) nitrate nonahydrate were used as starting materials. Aqueous solutions of metal nitrates were mixed with 5 mol % of lithium ions in excess comparing the required stoichiometric molar ratio. The lithium cations were added in excess in order to avoid the formation of hematite that was found to appear as a second phase when the cation molar ratio followed stoichiometric ratio. In the next step, the citric acid was added to the precursor solution with the metal to citric molar ratio of 1: 1. The solution was mixed and than slowly dried in an oven at 353 K for 12 h in order to undergo dehydration. After cooling down to room temperature the dried gel was sintered at 453 K for 12 h in order to induce gel decomposition. As-prepared sample (S1) was further annealed in air for 4 h at 573 K (S2), 673 K (S3), and 973 K (S4).

2.2. Experimental Methods. In order to check the stoichiometry of the samples, chemical quantitative analysis was performed using inductively coupled plasma optical emission spectroscopy (ICP-OES), Spectroflame ICP, 2.5KW, 27 MHz. The ICP-OES analysis was performed by measuring the intensity of radiation of the specific wavelengths emitted by each element. The samples were dispersed in liquid and introduced into the plasma in the form of aerosol, where they were vaporized, atomized, and excited.

Thermal analysis (DTA/TGA) was used to check the end of the decomposition process and to study changes of the order−disorder structural phase transition temperature with annealing. Measurements were done in air, in the temperature range from 300 to 1123 K, with a heating/cooling rate of 20 K/min, using TA SDT 2960 instrument.

Structural and microstructural analysis of nanocrystalline lithium ferrites (S1, S2 and S3) have been carried out using synchrotron based high-energy X-ray powder diffraction data (HEXRPD), whereas the X-ray powder diffraction data (XRPD) of bulk-like sample (S4) was collected on a Bruker D8 diffractometer in the angular range 13−113° (2θ) with a step of 0.017° and a counting time of 10 s per step. The particle size and shape of the sample S1 were determined by transmission electron microscopy (TEM) with a FEI TECNAI G2 30F microscope operated at 300 kV. To this purpose the powder particles have been dispersed on a holey carbon support film.

The HEXRPD experiments were performed at the 6-ID-D beamline at the Advanced Photon Source at Argonne National Laboratory, Argonne, Illinois. Diffraction data were collected using the recently developed rapid acquisition pair distribution function (RAPDF) technique[8a] that benefits from two-dimensional (2D) data collection. The powder samples were packed in Kapton capillaries with diameter of 1.0 mm, sealed at both ends. The data were collected at room temperature with an X-ray energy of 86.8406 keV (λ = 0.142773 Å) selected using Si (331) monochromator. Incident beam size was 0.6 × 0.6 mm. An image plate (IP) camera (Mar345) with a diameter of 345 mm was mounted orthogonally to the beam path with a sample to detector distance of 230.274 mm, as calibrated by using ceria standard sample.[8a] Each sample was exposed for 120 s and this

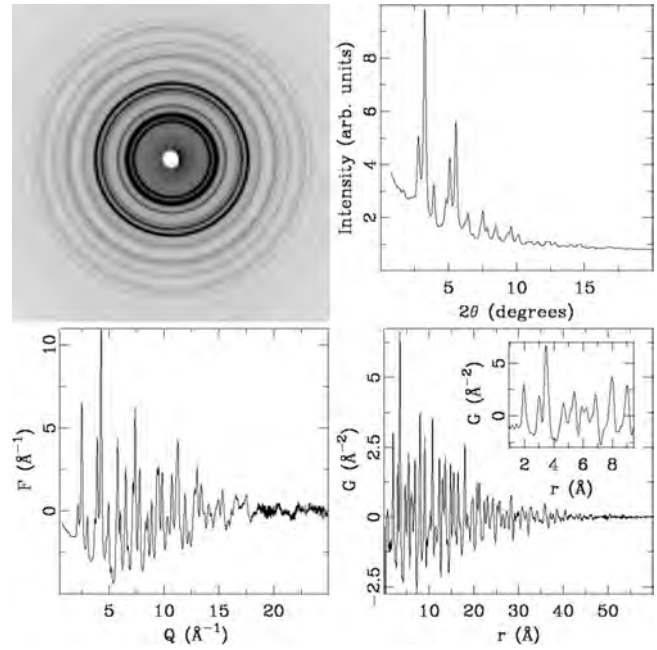

Figure 1. Experimental data obtained at 6-ID-D at APS for S1 sample at 300 K: 2D diffraction pattern (upper left), corresponding integrated 1D diffraction pattern (upper right), total scattering structure function, $F(Q)$, (lower left), and the atomic PDF (lower right). The inset shows a close-up to the low-r region in the PDF. The PDF intensity at high-r diminishes both as a result of the finite size of the nanoparticles, and due to the limited resolution of the 2D measurement.

was repeated 5 times for a total data collection time of 600 s. The RAPDF approach avoids detector saturation while allowing sufficient statistics to be obtained. To reduce the background scattering, lead shielding was placed before the sample with a small opening for the incident beam. Examples of the raw 2D data, for S1 sample are shown in top left panel of Figure 1. These data were integrated and converted to intensity versus 2θ using the software FIT2D,[8b] where 2θ is the angle between the incident and scattered X-ray beams. Example for S1 is shown in top right panel of Figure 1. The integrated data were normalized by the average monitor counts. The data were corrected and normalized[8c] using the program PDFgetX2[8d] to obtain the total scattering structure function, $F(Q)$ and its Sine Fourier transform, i.e. the atomic PDF, $G(r)$, which are shown respectively in bottom left and bottom right panels of Figure 1 for sample S1. In the Fourier transform of $F(Q)$ to get the PDF, $G(r)$, the data are truncated at a finite maximum value of the momentum transfer, $Q = Q_{max}$. Q_{max} is optimized such as to avoid large termination effects and to reasonably minimize the introduced noise level as the signal-to-noise ratio decreases with the increased Q value. Here, a Q_{max} = 27.0 Å^{-1} was found to be optimal.

Structural and microstructural analysis have been done from as collected XRPD data using the Rietveld profile refinement method[9a,b] incorporated into the program Fullprof[9c,d] and the PDF approach, using the program PDFgui.[8e] The obtained results were compared.

Mössbauer spectra were recorded at room temperature using MS4 Mössbauer spectrometer, operating in constant acceleration mode. The source was ^{57}Co in Rh matrix. The velocity calibration was done using natural iron foil.

3. Results and Discussion

3.1. Synthesis. The chemical composition of samples S1 and S4 has been checked by ICP-OES analysis. In the as-prepared

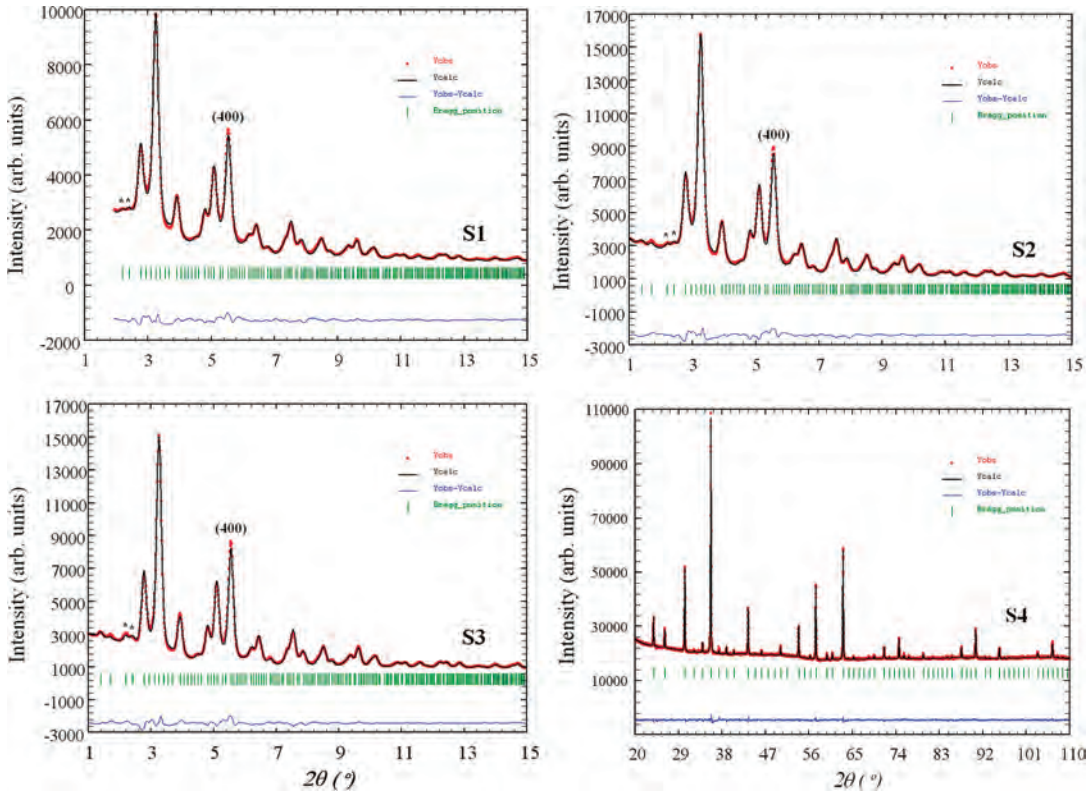

Figure 2. HEXRPD patterns of lithium ferrite: as-prepared (S1), annealed at 573 K (S2), and 673 K (S3), and XRPD pattern of sample annealed at 973 K (S4). Superstructure reflexions (210) and (211) are denoted by asterisk. Experimental data (Y_{obs}), refined XRPD spectrum (Y_{calc}) (S.G. $P4_332$), their differences ($Y_{obs} - Y_{calc}$), and the Bragg reflections' positions are shown in figure. Note that the data for S4 sample were collected in an experimental setup having much higher resolution than that used for S1, S2, and S3 samples and that the diffractograms are not directly comparable.

sample (S1), a deviation from the stoichiometry has been found, whereas in the sample S4 the molar ratio of Li/Fe ions with (1.68 ± 0.04) wt % of Li^+ and (65 ± 2) wt % of Fe^{3+} ions, corresponds to the required stoichiometric ratio for pure lithium ferrite phase. DTA analysis of sample S1 revealed that a mass lost of about 17% occurs in sample S1 with annealing up to 1123 K. This suggests the presence of some non decomposed organic part in the sample after thermal treatment of precursor gel at 453 K. Notable mass change is absent in samples S2 and S3.

The HEXRPD patterns of samples S1, S2, and S3 are shown in Figure 2. Their characteristic feature is the presence of low intensity superstructure reflections (210) and (211), which confirms that the samples crystallize in (at least partially) ordered spinel structure, S.G. $P4_332$. The presence of any other crystalline phase was not observed from the XRPD patterns. It is relatively common to find some impurity phase, usually hematite (α-Fe_2O_3), during the synthesis route via citrate precursor gel decomposition[10] or via oxalate precursor route.[11] We have found that the formation of α-Fe_2O_3 (~4 wt %) can be avoided by the use of an overstoichiometric solution where 5 wt % of lithium ions were added in excess during formation of precursor gel.

Detailed analysis of $Li_{0.5}Fe_{2.5}O_4$ preparation by the citrate gel precursor method has been recently reported.[12] It was pointed out that the decomposition/oxidation rate of anhydrous precursor can be crucial in order to avoid formation of impurities and that it can be controlled by setting up the pH value of the precursor. Higher pH value allows for a higher oxidation rate, which is necessary to obtain pure lithium ferrite phase, but at the same time it significantly increases the particles size. By keeping pH value near 1 and by adding some lithium in excess we have managed to obtain pure lithium ferrite phase.

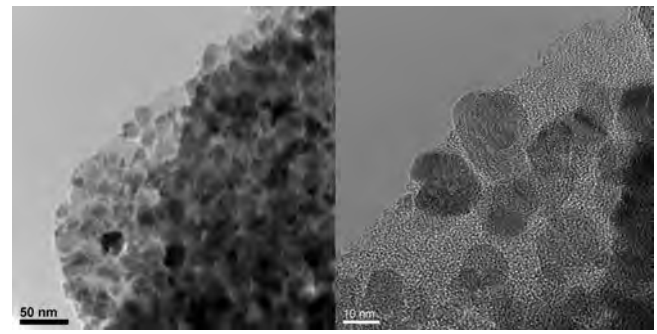

Figure 3. HRTEM micrographs of sample S1.

3.2. Crystal Structure and Microstructure of Nanocrystalline $Li_{0.5}Fe_{2.5}O_4$. ***3.2.1. TEM Analysis.*** High-resolution TEM (HRTEM) analysis provided more detailed structural information. From the HRTEM micrographs of sample S1, shown in Figure 3, we can see that the ferrite particles have globular morphology with the particle sizes laying in the range 10−20 nm. These values are something higher than the one determined by HEXRPD (~5 nm for samples S1 and S2, ~9 nm for sample S3; see lately in the text). Since the HEXRPD is sensitive to the size of the optically coherent volume, this discrepancy can indicate the presence of some residual defects in the S1 sample, which is fully recovered in samples heat treated at the highest temperature. Despite the possible presence of defects, HRTEM images also show that the particles seem to be single-crystalline in the nature. For soft ferrites, like lithium ferrite, it has been found that the critical particle size below which they are single-domain is about 30−40 nm.[13]

TABLE 1: Lattice Constant, the Fractional Coordinates of Oxygen O2 at the General 24e and Oxygen O1 at the Special 8c Positions, As Well As Lithium/Iron at the 12d and Iron at the 8c Sites, and the Average Crystallite (Particle) Size and the Max-Strain for Nanocrystalline $Li_{0.5}Fe_{2.5}O_4$ Annealed at 453 K (S1), 573 K (S2), and 673 K (S3), Obtained Using Rietveld (FP) and the Atomic PDF Approaches

sample	method	a (Å)	O2*x* (24e)	O2*y* (24e)	O2*z* (24e)	O1*x* (8c)	Li2/Fe2*y* (12d)	Fe3*x* (8c)	average crystallite size (Å)
S1	FP	8.3466(3)	0.1099(10)	0.1294(9)	0.3787(11)	0.3851(11)	0.3627(3)	0.9915(3)	54
	PDF	8.3499(38)	0.1180(11)	0.1207(10)	0.3809(15)	0.3731(14)	0.3669(5)	0.9973(5)	57(1)
		FP: $\chi^2 = 1.15$, $R_{Bragg} = 2.74$, $R_p = 1.95$; PDF: Reduced $\chi^2 = 0.035$; $R_w = 0.134$; Max-strain (10^{-4}) = 34.0(0.5)[a]							
S2	FP	8.3205(3)	0.1101(10)	0.1300(8)	0.3781(12)	0.3842(11)	0.3638(3)	0.9930(3)	54
	PDF	8.3243(6)	0.1194(10)	0.1208(9)	0.3804(13)	0.3813(12)	0.3681(5)	0.9983(5)	59(1)
		FP: $\chi^2 = 2.22$, $R_{Bragg} = 2.63$, $R_p = 2.34$; PDF: Reduced $\chi^2 = 0.045$; $R_w = 0.118$; Max-strain (10^{-4}) = 29.2(0.4)[a]							
S3	FP	8.3337(2)	0.1120(11)	0.1321(8)	0.3774(10)	0.3837(12)	0.3660(3)	0.9942(3)	87
	PDF	8.3385(14)	0.1143(9)	0.1239(7)	0.3804(12)	0.3718(12)	0.3692(5)	0.9992(5)	94(1)
		FP: $\chi^2 = 1.93$, $R_{Bragg} = 3.02$, $R_p = 2.28$; PDF: Reduced $\chi^2 = 0.046$; $R_w = 0.101$; Max-strain (10^{-4}) = 28.8(0.4)[a]							

[a] Numbers in parentheses have meaning of degree of anisotropy (not standard deviation).

3.2.2. Rietveld vs PDF Method. The comparative crystal structure and microstructure analysis of $Li_{0.5}Fe_{2.5}O_4$ samples annealed at different temperatures have been performed by two methods: by full profile Rietveld refinement using program Fullprof ([13]c), and by the PDF method.[8c,14] The two complementary approaches were chosen, as it is well-known that crystal structure analysis of nanoparticle materials is subject to numerous difficulties when using conventional powder diffraction methods alone. These methods can become insufficient or even break down as the diffuse scattering becomes significant at the nanoscale, while the Bragg scattering, the one that crystallography relies upon, gets diminished. As an alternative, the total scattering based atomic PDF method is one of the promising experimental approaches in nanoscale structure determination, particularly when used in combination with other techniques that provide highly complementary information.[14b]

The full profile Rietveld method allows the average structure determination from the Bragg peaks position and intensity, and the microstructure determination (size-strain analysis) from the peak profile analysis.[9a,b] XRPD peak profiles are modeled by the Thomson-Cox-Hasting modified pseudo-Voigt (TCH-pV) function and the instrumental resolution function is used to estimate the microstructural parameters (the average crystallite size and microstrain). The Fullprof program package allows for an estimate the average crystallite size and microstrain by averaging the values obtained for apparent size and maximum strain calculated for each crystal direction [hkl] given by expressions:[9c] Apparent size $= 1/\beta_{size}$ (Å) and Max-strain $= (\beta_{strain} d_{hkl}/2)$ ($\times 10^{-4}$). In the case of isotropic size and strain models, both β_{size} and β_{strain} were obtained from TCH-pV functions parameters according to procedure described in ref 9c.

In the diffraction patterns of nanocrystalline materials diffuse scattering is more dominant than in those of crystalline materials, hence using PDF analysis of neutron and X-ray total scattering data comes as a natural choice for studying the structure of nanostructured materials.[8a,c,14a] Recently, the structure of discrete nanoparticles has been successfully studied using this approach.[15–19] If special care is applied to the measurement and to the approach used for analyzing the data, the PDF method can yield precise structure and size information. The atomic PDF, $G(r)$, is defined as $G(r) = 4\pi r[\rho(r) - \rho_0]$, where $\rho(r)$ is the atomic pair density, ρ_0 is the average atomic number density, and r is the radial distance.[8c] The PDF yields the probability of finding pairs of atoms separated by a distance r. It is obtained by a Sine Fourier transformation of the reciprocal space total scattering structure function, $F(Q) = Q[S(Q) - 1]$, according to $G(r) = (2/\pi)\int_0^\infty F(Q) \sin(Qr)\, dQ$, where $S(Q)$ is obtained from a diffraction experiment. This approach is widely used for studying liquids, amorphous, and crystalline materials, and has recently also been successfully applied to characterize nanocrystalline materials.[14c]

3.2.3. Rietveld Approach. The HEXRPD patterns of nanocrystalline lithium ferrite annealed at 453, 573, and 673 K (S1, S2, and S3, respectively) are shown in Figure 2. As already mentioned, all samples were found to crystallize in a cubic spinel structure, and the presence of superstructure reflections indicates cation ordering within the octahedral sublattice (S.G. $P4_332$). Compared to diffraction pattern of standard powder (CeO_2), broadening of diffraction peaks due to the small crystallite size and the effects of strain is observed. The Rietveld refinement has been performed within the space group $P4_332$ using the Fullprof program. The isotropic size and strain model[9c] is applied, and the results of refinements are presented in Table 1.

The starting model for crystal structure refinement of samples S1, S2, and S3 was based on a bulk-like cation distribution model in which the tetrahedral, 8c sites are occupied only by Fe^{3+} ions and the rest of Fe^{3+} ions and all Li^+ ions are distributed between two distinct octahedral sites, 4b and 12d, in the space group $P4_332$. The best refinements were obtained when a partial mixing of Li^+ and Fe^{3+} ions between two octahedral sites, 4b and 12d, was allowed. Since Li scatters X-rays poorly compared to the heavier elements present in the structure, Li occupation is followed indirectly, by keeping Li occupation numbers constrained with those of Fe ions in order to preserve the proper Li/Fe ratio.

The refined patterns showed very good agreement with experimental data (Figure 2), except for a small difference between experimental and calculated intensity of (440) reflection. There can be several possible reasons for this deviation, all of them being specific to this material: the presence of short-range disordering along the [110] direction (direction of cation ordering in an ordered spinel structure), anisotropic microstrain due to dislocations, phase boundaries or stacking faults (the latter leads to asymmetric peaks),[20] and also surface relaxation effects, when the broad and even asymmetric tails can arise from the departure from crystalline order of the surface layers.[6b]

Following the model described above, we have found an insignificant change in the cation distribution with annealing up to 673 K. The occupancy of 4b site by lithium in all nanocrystalline samples was found to vary around 60% of overall Li content, and so the cation distribution can be represented by the formula $(Fe^{3+})_{8c}[(Li^+_{0.3}Fe^{3+}_{0.2})_{4b}(Li^+_{0.2}Fe^{3+}_{1.3})_{12d}]$. The samples S1, S2, and S3 may be therefore regarded as a partially

ordered. These results reflect the importance of particular synthesis route for nanoparticle lithium ferrite. For instance, it was found that the citrate gel method used with ammonia solution added into the precursor, produces a random distribution of Li^+ ions over the octahedral and tetrahedral sites, S.G. $Fd\bar{3}m$.[21] After annealing at 973 K, a totally ordered lithium ferrite $(Fe^{3+})_{8c}[(Li^{+}_{0.5})_{4b}(Fe^{3+}_{1.5})_{12d}]$ has been obtained (sample S4).

The important structure and microstructure parameters obtained from Rietveld method are summarized in Table 1. When analyzed in terms of annealing temperature, these results show some differences in behavior of structural (unit cell and atomic parameters) and microstructural (size and strain) parameters. While microstructure parameters seem to change in adequate manner (increase of particle size with temperature and decrease of average microstrain), the values of structure parameters, in particular the cell constants show a nonuniform change with annealing temperature.

Compared to the bulk form of fully ordered lithium ferrite (S4), the cell constants of S1 and S2 were found to be over- and underestimated, respectively. Similar values of these parameters were also obtained by PDF method (for comparison, they are also given in Table 1). Apart from the possible limitations of the applied structural model itself (bulk-like description of the crystal structure), the explanation for discrepancy between unit cell values of S1 and S2 can also be found in specific behavior of the microstructure parameters for these two samples. Their values reveal that annealing at 573 K does not induce significant change in particle size but predominantly results in the reduction of microstrain, which is known to increase the lattice constant in nanosized samples compared to their bulk counterpart.[7] Thus the higher defect concentration and/or the mixing effects of both micro- and macrostrain are likely to contribute to the increased value for S1 cell constant. However, as annealing at 573 K leads to decreased value of unit cell constant in S2, this value is found to be somewhat smaller than the one related to bulk lithium ferrite, which suggests that this effect is not possible to explain only in terms of average defect relaxation estimated from the Rietveld analysis. The PDF analysis, on the other hand, reveals existence of oxygen disordering in the samples, and provides additional insight into the short-range structure that is generally out of the scope of the Rietveld method. We describe these results below.

3.2.4. PDF Approach. Here, we apply the PDF method to study the structure and size in lithium ferrite nanoparticles, where the size is controlled by adjusting the temperature in the annealing step of the synthesis, as described. Figure 4 features experimental PDFs, shown as open circles, for the three samples used. From Figure 4 is apparent that, in direct space, the PDF features at low r are comparably sharp in all the samples. Unlike in the reciprocal space, the direct space features are not broadened due to the finite size effects. The finite particle size produces a falloff in the intensity of structural features with increasing interatomic spacing r, similar to one that can be seen in the lower right panel of Figure 1. The structure apparent in the $G(r)$ function, as that seen in Figure 4, comes from the atomic order within the nanoparticle. In case of high reciprocal resolution measurements on nanoparticle samples, the value of r where the PDF signal disappears indicates the particle *core* region diameter, or at least the diameter of any coherent structural core of the nanoparticle. Features in the PDF at low r reflect the internal structure of the nanoparticles. Inspection of the experimental PDF data in Figure 4 reveals that nanoparticles have almost the same features, reflecting the fact that they

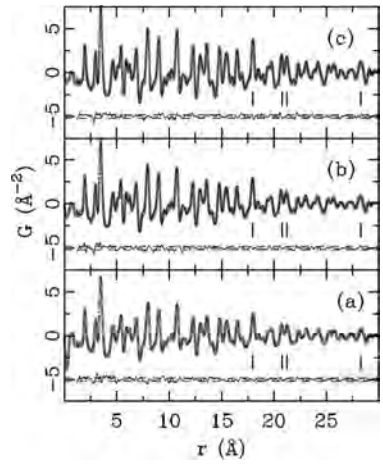

Figure 4. PDFgui refinements of the $P4_332$ model to the experimental PDF data for (a) S1 sample, (b) S2 sample, and (c) S3 sample, over a wide r-range. Data are shown as open symbols, model profiles as solid lines, and corresponding difference curves are shown offset below for clarity. Dashed horizontal lines denote estimated experimental uncertainty at 2σ level. All profiles shown in panels (b) and (c) are placed on the same scale as in (a) for easier comparison. Vertical tick marks denote selected features discussed in the text.

share a similar atomic structure on average. In the finite nanosize regime, local structural changes are expected: the largest changes in structure are expected in the smallest nanoparticles. In such nanoparticles, the contribution of surface atoms is large, making it difficult to define well-ordered crystalline core. It should be noted here that the effect of limited reciprocal space resolution of the measurement also yields a similar falloff of the PDF intensity, producing a Gaussian envelope to the experimental PDF. In studying crystalline materials, distinct are sample (grain size effect) and resolution limited measurements, depending on which of the effects is predominant.[8c] Since the resolution effects necessarily come to play when IP detectors are used, and are relevant in case of intermediate size nanoparticles, such as these studied here, measurements on silicon crystalline standard were carried out to account for this, as explained below.

Using the PDF approach, it is possible to obtain size-dependent quantitative structural information, and through a structure modeling process refine reliable structural parameters, even in cases of very small nanoparticles.[19] Structural information was extracted from the PDFs using a full-profile real-space least-squares refinement approach, analogous to the Rietveld refinement. We used the program PDFgui[8e] to fit the experimental PDFs. Starting from a given structure model and given a set of parameters to be refined, PDFgui searches for the best structure that is consistent with the experimental PDF data. The residual function, R_w, is used to quantify the agreement of the calculated PDF from model to experimental data, and is minimized in the refinement process. The structural parameters of the model (cubic, $P4_332$) were: lattice parameter, fractional coordinates observing $P4_332$ symmetry constraints, isotropic atomic displacement parameters (ADPs), and the site occupancy of Li atom. The modeling program takes into account both the particle size and the finite resolution effects, through corresponding fitting parameters.[8c,14c] The resolution damping factor, Q_{damp}, which defines PDF Gaussian dampening envelope $(0.5e^{-(Q_{damp}\cdot r)^2})$ due to limited Q-resolution,[8c,e] was determined from a refinement to the silicon standard data and fixed, and the nanoparticle diameter was refined. PDF data obtained for Si standard (325 mesh) are shown in Figure 5a with dampening envelope superimposed, highlighting the effect of the resolution

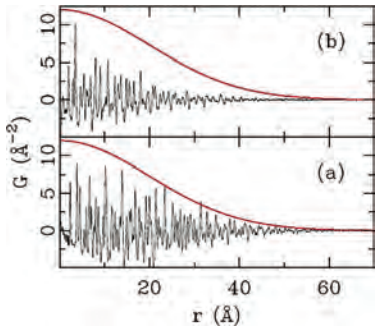

Figure 5. Effect of reciprocal space resolution on PDF. (a) Silicon standard PDF (solid line profile) and PDF Gaussian dampening envelope (thick solid line) scaled to track the data. (b) PDF of sample S1 (solid line profile) with the same envelope as shown in (a). Data shown in (a) and (b) are on the same scale. See text for details.

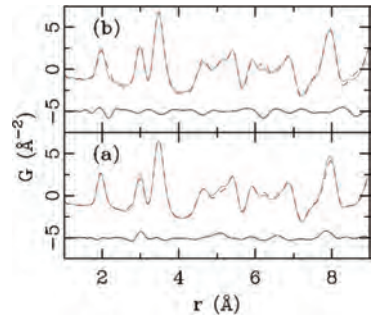

Figure 6. Effect of disorder on PDF. (a) Model PDF (solid line profile) for S1 sample with the occupancy of Li on octahedral 4b site set to 0.50 as observed in the bulk counterpart, and model PDF (dashed line profile) with the occupancy of Li set to 0.1. (b) Model PDF (solid line profile) for S1 sample with ADP of O1 set to observed unphysically large values, and model PDF (dashed line profile) with ADP of O1 set to physically reasonable values comparable to that obtained for O2. In both panels difference curves are offset for clarity. See text for details.

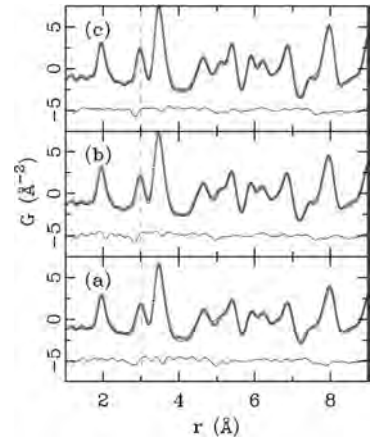

Figure 7. PDFgui refinements of the $P4_332$ model to the experimental PDF data for the (a) S1, (b) S2, and (c) S3 samples, over a narrow *r*-range. Dashed vertical lines denote position of the second PDF peak in the data, to emphasize the data-model mismatch, as also evident in the difference curve. All profiles shown in panels (b) and (c) are placed on the same scale as in (a) for easier comparison. See text for details.

of IP measurement on data. For comparison, PDF data for S1 sample are shown in Figure 5b, demonstrating sensitivity to additional dampening observable in these data originating from the finite size of the nanoparticles. This is particularly obvious in the 30−50 Å region, where PDF peaks of Si are much stronger than PDF peaks of S1 sample. Good agreement, with low values of R_w, between the model and the data was achieved for all three samples. The fits are shown in Figure 4 as model PDFs (solid lines) superimposed on data, with the difference curves offset for clarity. Vertical tick marks label selected features in the PDF, allowing for visual comparison of these PDF peaks. Notably, higher-*r* features are more dampened and additionally broadened for samples S1 and S2, compared to that for sample S3, landing confidence that different nanoparticle sizes can be distinguished and assessed from the modeling process despite resolution effects. The obtained structural parameters are reported in Table 1.

Determining accurately the occupancy of Li represents a challenge for the reasons already stated in the previous section. PDF refinements were carried over two ranges, narrow (up to ∼10 Å) and broad (spanning available PDF data up to ∼50 Å). Notably, in all PDF refinements, the occupancy of Li on octahedral 4b site refined to lower values compared to 0.50 observed in the bulk counterpart. This was persistently observed for all three samples, indicating that an appreciable amount of Li ions occupy the octahedral 12d sites. Broad range fits were initially unstable, due to correlation between Li occupancy and ADP parameters of lithium and oxygen ions. Therefore, in the final refinements over a broad range, the Li occupancy was set to 0.2(1), as obtained from more stable fits for S3, and fixed for all three samples, which gave satisfactory fits. Interestingly, when the refinements were carried over a narrow range, the observed Li occupancy on the 4b site indicated even smaller values (below 0.1), suggesting a possibility that some of the Li ions escape to the outer layers of the nanoparticles. An idea about the sensitivity of PDF to this effect can be gained from Figure 6a, where two model PDFs for Li occupancy observed in the bulk, and that reported in this study are compared. Quantifying this, however, is beyond the sensitivity of our measurement.

We also found a significant difference in the fractional coordinates of oxygen ions in 8c site (O1) and 24e site (O2) depending on whether PDF or Fullprof methods were used. In conjecture with this is another observation that we made: an anomalous increase of the O1 isotropic ADP parameters to unphysical values, for all three samples, whereas the ADPs of other sites were having considerably smaller values, albeit still enhanced. This is suggesting significant disorder in the O1 network, that appears to be the largest for the smallest nanoparticle (S1), with ADP of O1 being 0.148(5) Å^2, compared to 0.128(5) Å^2 and 0.140(5) Å^2 for S2 and S3 samples, respectively. For comparison, observed ADP values for O2 site are 1 order of magnitude smaller, being 0.012(1), 0.010(1), and 0.011(1) Å^2 for S1, S2, and S3, respectively. Illustration of the effect of disorder in the O1 sublattice is provided in Figure 6b by comparing model PDFs corresponding to anomalously increased and more physical values of O1 ADPs.

From the PDF fits over the narrow *r*-range (Figure 7), apparent discrepancies between the model and the data in the PDF peak position of certain peaks can be observed. The figure features fits to the data of the (a) S1, (b) S2, and (c) S3 samples. For easier comparison, all of the profiles in the later two panels were rescaled such to be on the same scale as these shown in panel (a). Vertical dashed lines denote the position of the second PDF peak of the data, emphasizing that there is an offset between the data and the model peak, also evident in the difference curve. Such mismatch also occurs for some other PDF peaks, as evident from the difference curves. This is consistent with there being a shell region where the interatomic

TABLE 2: Cation−Anion Distances Which Correspond to the Refined Crystal Structure Parameters by the Rietveld (FP) and PDF Methods[a]

sample	method	$\langle d_{8c\text{-}O^{2-}}\rangle$ (Å)	$d_{4b\text{-}O^{2-}}$ (Å)	$\langle d_{12d\text{-}O^{2-}}\rangle$ (Å)
S1	FP	1.892(10)	2.151(12)	2.014(12)
	PDF	1.863(11)	2.053(10)	2.060(10)
S2	FP	1.886(10)	2.126(10)	2.011(10)
	PDF	1.880(8)	2.047(9)	2.035(9)
S3	FP	1.870(10)	2.145(9)	2.022(10)
	PDF	1.856(8)	2.078(9)	2.052(9)
$(Fe^{3+})_{8c}[(Li^{+}_{0.3}Fe^{3+}_{0.2})_{4b}(Li^{+}_{0.2}Fe^{3+}_{1.3})_{12d}]O_4$	calc.	1.87	2.178	2.059

[a] Label "calc." denotes values of cation−anion distances related to the given cation distribution and Shannon−Prewitt effective ionic radii.

distances are different than those in the core. There is no evidence in PDF that the shell is amorphous, which would manifest itself as a set of glass-like PDF features in the difference curve, with sharp near-neighbor distances, and a disordered hump at higher values of r. The data are more consistent with the shell being crystalline, with somewhat disordered structure, but similar to that of the core. The resolution (falloff) effects hamper the ability to estimate the spatial extent of the core and shell regions from the PDF analysis.

3.2.5. Analysis of Cation−Anion Distances. As two methods (Rietveld and PDF) give an appreciable mismatch in fractional coordinates of oxygen ions in 8c (O1) and 24e sites (O2) (Table 1), we compared the cation−anion distances (given in Table 2), which correspond to the refined crystal structure parameters obtained by Rietveld (FP) and PDF methods, with the values calculated from the effective ionic radii and refined cation distribution.[22] The average cation−anion distances for 8c and 12d sites obtained by Fullprof and PDF are in agreement within three estimated standard deviations (ESD), whereas notable deviation is found for 4b site. Further, the average cation(8c)−anion distance (obtained by Fullprof and PDF) match pretty well value 1.87 Å calculated from Shannon effective ionic radii in the case that 8c site is occupied only by Fe^{3+} ions. The average cation(12d)−anion distances are also in agreement with value calculated taking into account the cation distribution ($(Li^{+}_{0.2}Fe^{3+}_{1.3})_{12d}$) and ionic radii. This supports obtained refinement results when so-called bulk-like model was applied in nanocrystalline lithium ferrites. Some discrepancies are found only for 4b site where the cation(4b)−anion distances appears somewhat shorter (especially those obtained by PDF), from the predicted value calculated concerning the cation distribution ($(Li^{+}_{0.3}Fe^{3+}_{0.2})_{4b}$). Regarding the value of Li^{+} and Fe^{3+} (high spin) ionic radii in octahedral coordination, this discrepancy could be an indication of some migration of Li ions from 4b sites to outer surface layers.

3.3. Mössbauer Spectroscopy of $Li_{0.5}Fe_{2.5}O_4$. Fe^{57} Mössbauer spectra for all samples were recorded at room temperature (Figure 8). The Mössbauer spectrum of sample S4 could be fitted with two overlapping sextets, assigned to Fe^{3+} ions at tetrahedral (A) and octahedral (B) sites. The Mössbauer parameters (isomer shift $\delta \cong 0.22$ and 0.37 mm s^{-1}, and hyperfine fields $B_{hyp} = 50.3$ and 51.0 T for A and B sites, respectively) are in agreement with previous results of $H_A = 50.0$ T, $\delta_A \cong 0.20$ and $H_B = 50.6$ T, $\delta_B \cong 0.37$ mm s^{-1} for A and B sites, respectively.[23] Dormann et al.[24a] have suggested that zero-field Mössbauer spectra of lithium ferrite taken at $T = 78$ K can be used to determine the relative Fe ion occupation

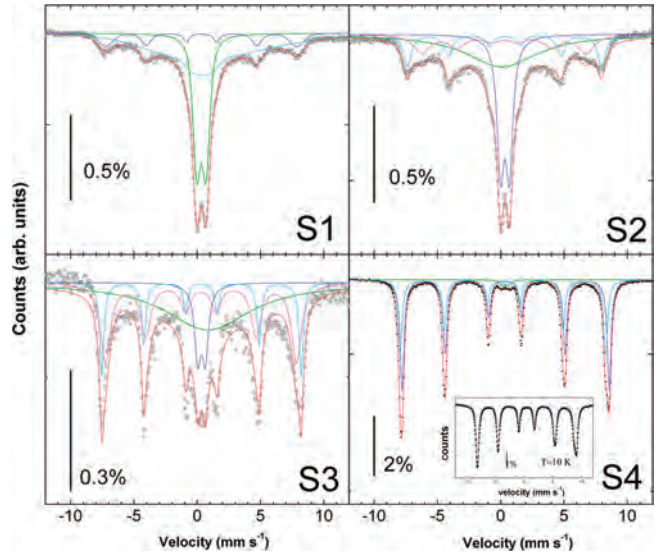

Figure 8. Mössbauer spectra of all samples (S1−S4) collected at room temperature.

at A and B sites. The ratio of spectral areas corresponding to Fe^{3+} at A and B sites was obtained from Mössbauer data taken at $T = 10$ K (see the inset of Figure 8), and the obtained value was in agreement with the ordered $(Fe^{3+}_{8c})_{tet}[(Li^{+}_{0.5})_{4b}(Fe^{3+}_{1.5})_{12d}]_{oct}$ cation distribution inferred from Rietveld refinement sample S4.

The room temperature Mössbauer spectra recorded for samples with smaller particle size (namely, S1, S2, and S3) could be fitted using two sextets and one broad doublet, the latter originating from the superparamagnetic relaxation of the smallest nanoparticles. This coexistence of sextets/doublets is typical for samples of ultrafine particles with size distributions, due to the exponential dependence of the relaxation time τ with particle volume.

For particles having relaxation times τ larger than the Larmor precession time $\tau_L \approx 10^{-8}$ s of the resonant ^{57}Fe nucleus, the later can sense the magnetic hyperfine interactions resulting in a magnetically split sextet. On the other hand, particles having $\tau < \tau_L$ will fluctuate many times during the time scale of the ^{57}Fe excited state, averaging all interactions to zero and leaving the quadrupolar interactions alone. Near the condition $\tau \approx \tau_L$ (i.e., the blocking temperature T_B for Mössbauer time window) the typical Mössbauer spectrum usually consists of a paramagnetic doublet superimposed on a magnetic hyperfine sextet, the latter exhibiting broad absorption lines and reduced hyperfine splitting. Since there are no theoretical models for the resulting Mössbauer spectra for $\tau \approx \tau_L$ (neither lineshapes nor hyperfine field behavior), the interpretation of any hyperfine parameter from spectra near T_B must be done with caution.

In our samples, the intensity of the central doublet originating from superparamagnetic relaxation of smaller particles decreases with increasing the annealing temperature and the magnetically split sextet becomes the major fraction of the ^{57}Fe signal, as expected from the growth of the average particle size. Concurrently, the spectral lines narrow for samples with higher annealing temperatures, due to the increase of average particle sizes and/or improved crystallinity of the particles. Table 3 summarizes the fitted Mössbauer parameters for lithium ferrite. It is worth mentioning that no indication of Fe^{2+} spectral component was detected in our samples.

The Mössbauer parameters obtained for bulk-like sample S4, namely 50.3 and 51.0 T (A and B sites, respectively) are in

TABLE 3: Hyperfine Parameters Obtained from Fits to the ^{57}Fe Mössbauer Spectra Collected at Room Temperature for Samples S1−S4[a]

sample	component	δ (mm s^{-1})	QS (mm s^{-1})	B_{hyp} (T)
S1	doublet	0.33	0.74	
	sextet A	0.27		31
	sextet B	0.33		46.9
S2	doublet	0.33	0.69	
	sextet A	0.27		40.1
	sextet B	0.30		47.6
S3	doublet	0.33	0.59	
	sextet A	0.29		46.8
	sextet B	0.33		48.6
S4	sextet A	0.22	−0.03	50.3
	sextet B	0.37	0.01	51.0

[a] The parameters are isomer shift (δ), quadrupole splitting (QS), and hyperfine field (B_{hyp}).

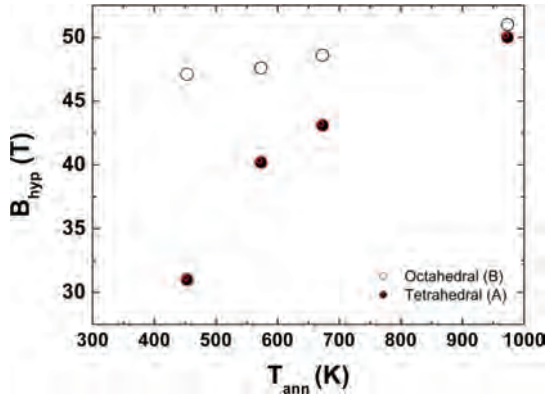

Figure 9. Hyperfine fields (B_{hyp}), for Fe^{3+} ions at tetrahedral (A) and octahedral (B) sites in spinel lattice.

agreement with previous reports on this system.[23] It is interesting to note that the evolution of hyperfine fields of A and B sites for Fe^{3+} ions with annealing temperatures are quite different (Figure 9). Indeed, the hyperfine field of the tetrahedral site shows a marked decrease for samples annealed at lower temperatures, reflecting larger sensitivity to changes in the local environment and/or to relaxation effects of the single-domain particles.

For NPs with different cation distributions at the cores and surface layers, fitting of the Mössbauer spectra by using multiple sextets (up to five) is impractical.[23] The complexity of the spectra in nanocrystalline $Li_{0.5}Fe_{2.5}O_4$ samples is due not only to relaxation effects near the SPM transition, but also due to the complex cation distribution. Previous studies have proposed detailed models for fitting substituted bulk lithium ferrite (e.g., Cr-doped $Li_{0.5}Fe_{2.5}O_4$) using multiple sets of subspectra, based on a model of supertransferred hyperfine field contributions at each Fe site.[24] In any case, the observed broadening of the sextet lines are the previous stage before SPM relaxation takes place, and therefore it seems more plausible to relate both the observed hyperfine field decrease and line broadening to Néel relaxation effects in single-domain nanoparticles.

3.4. Order−Disorder Phase Transition in $Li_{0.5}Fe_{2.5}O_4$. DTA analysis was used to investigate structural phase transitions (S.G. $P4_332 \leftrightarrow Fd\bar{3}m$), in all prepared samples, and the corresponding DTA curves are shown in Figure 10. DTA graph shows that each sample exhibits discernible endothermic peak which appears at $T_f' = 1033$ K in nanocrystalline samples (S1, S2, and S3) and at $T_f' = 1041$ K in bulk-like lithium ferrite (S4). This endothermic transition observed in heating regime, corresponds to the exothermic transition in cooling regime which

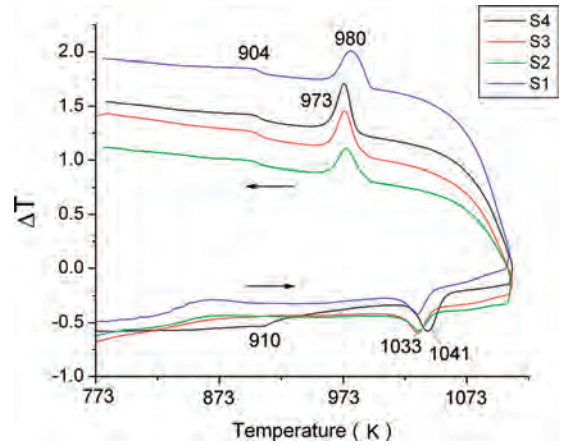

Figure 10. DTA curves of samples S1, S2, S3, and S4 measured in heating and cooling regimes (shown in the range of temperature 773−1110 K).

appears at $T_f'' = 980$ K in sample S1, and $T_f'' = 973$ K in samples S2, S3, and S4. Both observed types of transition peaks are due to reversible order−disorder phase transition in lithium ferrite and are shifted relative to each other (so-called thermal hysteresis) in heating/cooling regime: $\Delta T = T_f' - T_f'' \approx 53$ K for sample S1, ≈60 K for S2 and S3, and ≈68 K for S4, and these observations are consistent with the reported data.[25] Hence, lower driving force is necessary to induce order−disorder phase transition in nanocrystalline samples compared to their bulk counterpart, and consequently the temperature of phase transition in bulk sample is 8 K above the transition temperature in nanocrystalline samples.

DTA curves also exhibit a flexure at approximately 904 K, which can be related to a magnetic phase transition (ferrimagnetic ↔ paramagnetic). This transition occurs at the same temperature in all samples and is close to that one obtained from DSC measurements (920 K).[26] Literature value of the Nèel temperature of lithium ferrite is usually in the range of T_N = 913−953 K.[27]

4. Conclusions

In this paper we have analyzed certain aspects of synthesis of lithium ferrite obtained from citrate precursor gel decomposition at very low temperature, discussing the evolution of the crystal structure/microstructure parameters and Mössbauer parameters with annealing. The addition of 5 wt % of lithium in excess in citrate precursor enables the preparation of nanocrystalline lithium ferrite phase at 453 K, free from impurity ferric oxides. It has been found that annealing of the samples up to 673 K resulted in a similar atomic structure on average with almost unchanged cation distributions. Based on the analysis of the cation−anion distances, and within the precision given by XRPD technique, we suggest the possible migration of lithium ions from 4b sites to outer layers of particles. PDF analysis reveals an anomalous increase of the oxygen O1 isotropic ADP parameters to unphysical values, suggesting significant disordering in the O1 network. Mössbauer spectra of samples annealed at lower temperatures show decreased hyperfine field values, as expected from thermal fluctuations in small particles. With increasing annealing temperatures, the particles increase their average size and hyperfine fields increase to the bulk values. Taking into account that the nearest neighbor coordination of the iron in tetrahedral (A) sites is much more influenced by the oxygen O1 anions than the octahedral (B) sites in spinel structure, we can conclude that thermal annealing

of lithium ferrite powder mainly activated relaxations of the oxygen sublattices and does not change significantly the cation distribution up to 673 K. After annealing at 973 K, XRPD and Mössbauer experiments reveal that the sample S4 has a totally ordered cation distribution and bulk-like properties. The DTA analysis indicates that lower driving force is necessary to induce order−disorder phase transition in nanocrysalline samples compared to the bulk-like sample due to higher crystal disordering.

Acknowledgment. The Serbian Ministry of Science has financially supported this work through the project No. 141027. A.S.M. and E.S.B. thank SJL Billinge for useful discussions. Parts of this work were also supported by National Science Foundation (NSF) Grant Nos. DMR-0304391 and DMR-0703940. HEXRPD data were collected at the 6ID-D beamline at the Advanced Photon Source at the Argonne National Laboratory supported under DOE Contract No. DE-AC02-06CH11357. G.F.G. acknowledges financial help from Spanish MICINN through the Ramon y Cajal program.

References and Notes

(1) Baba, P. D.; Argentina, G. M.; Courtney, W. E.; Dionne, G. F.; Temme, D. H. *IEEE Trans. Magn.* **1972**, *MAG-8*, 83–94.

(2) Wang, X.; Gao, L.; Li, L.; Zheng, H.; Zhang, Z.; Yu, W.; Qian, Y. *Nanotechnology* **2005**, *16*, 2677–2680.

(3) Rezlescu, N.; Doroftei, C.; Rezlescu, E.; Popa, P. D. *Sens. Actuators B* **2008**, *133*, 420–425.

(4) Kato, E. *Bull. Chem. Soc. Jpn.* **1958**, *31*, 113–117.

(5) Antic, B.; Kremenovic, A.; Nikolic, A. S.; Stoiljkovic, M. *J. Phys. Chem. B* **2004**, *108*, 12646.

(6) (a) Nunes, A. C.; Yang, L. *Surf. Sci.* **1998**, *399*, 225–233. (b) Nunes, A. C.; Lin, D. *J. Appl. Crystallogr.* **1995**, *28*, 274–278.

(7) Widatallah, H. M.; Johnson, C.; Gismelseed, A. M.; Al-Omari, I. A.; Stewart, S. J.; Al-Harthi, S. H.; Thomas, S.; Sitepu, H. *J. Phys. D: Appl. Phys.* **2008**, *41*, 165006.

(8) (a) Chupas, P. J.; Qiu, X.; Hanson, J. C.; Lee, P. L.; Grey, C. P.; Billinge, S. J. L. *J. Appl. Crystallogr.* **2003**, *36*, 1342–1347. (b) Hammersley, A. P.; Svenson, S. O.; Hanfland, M.; Hauserman, D. *High Press. Res.* **1996**, *14*, 235. (c) EgamiT.; Billinge, S. J. L. *Underneath the Bragg Peaks: Structural Analysis of Complex Materials*; Cahn, R. W., Eds.; Pergamon: New York, 2003. (d) Qiu, X.; Thompson, J. W.; Billinge, S. J. L. *J. Appl. Crystallogr.* **2004**, *37*, 678. (e) Farrow, C. L.; Juhás, P.; Liu, J. W.; Bryndin, D.; Bozin, E. S.; Bloch, J.; Proffen, Th.; Billinge, S. J. L. *J. Phys: Condens. Matter* **2007**, *19*, 335219.

(9) (a) Rietveld, H. M. *J. Appl. Crystallogr.* **1969**, *2*, 65–71. (b) Young, R. A. *The Rietveld Method*; Oxford University Press: New York, 1993. (c) RodriguezCarvajalJ. FullProf computer program 2008 (http://www.ill.eu/sites/fullprof/index.html). (d) Rodríguez-Carvajal, J. Recent Developments of the Program FULLPROF, in Commission on Powder Diffraction (IUCr). *Newsletter* **2001**, *26*, 12–19. (http://journals.iucr.org/iucr-top/comm/cpd/Newsletters/).

(10) Verma, S.; Karande, J.; Patidar, A.; Joy, P. A. *Mater. Lett.* **2005**, *59*, 2630–2633.

(11) Hessien, M. M. *J. Magn. Magn. Mater.* **2008**, *320*, 2800–2807.

(12) Verma, S.; Joy, P. A. *Mater. Res. Bull.* **2008**, *43*, 3447–3456.

(13) Verma, S.; Joy, P. A. *J. Phys. D: Appl. Phys.* **2005**, *98*, 124312.

(14) (a) Billinge, S. J. L. *J. Solid State Chem.* **2008**, *181*, 1698–1703. (b) Billinge, S. J. L.; Levin, I. *Science* **2007**, *316*, 561–565. (c) Billinge, S. J. L.; Kanatzidis, M. G. *Chem. Commun.* **2004**, 749–760.

(15) Gilbert, B.; Huang, F.; Zhang, H.; Waychunas, G. A.; Banfield, J. F. *Science* **2004**, *305*, 651.

(16) Neder, R. B.; Korsunskiy, V. I. *J. Phys.: Condens. Matter* **2005**, *17*, S125.

(17) Zhang, H. Z.; Gilbert, B.; Huang, F.; Banfield, J. F. *Nature* **2003**, *424*, 1025.

(18) Petkov, V.; Peng, Y.; Williams, G.; Huang, B.; Tomalia, D.; Ren, Y. *Phys. Rev. B* **2005**, *72*, 195402.

(19) Masadeh, A. S.; Bozin, E. S.; Farrow, C. L.; Paglia, G.; Juhás, P.; Karkamkar, A.; Kanatzidis, M. G.; Billinge, S. J. L. *Phys. Rev. B* **2007**, *76*, 115413.

(20) Leoni, M.; Scardi, P. Surface Relaxation Effects in Nanocrystalline Powders. In *Diffraction Analysis of the Microstructure of Materials*; Scardi, P., Mittemeijer, E. J., Eds.; Springer Verlag: Berlin, 2003.

(21) Dey, S.; Roy, A.; Das, D.; Ghose, J. *J. Magn. Magn. Mater.* **2004**, *270*, 224–229.

(22) Shannon, R. D. *Acta Crystallogr.* **1976**, *A32*, 751–767.

(23) Kuznetsovy, M. V.; Pankhurst, Q. A.; Parkinz, I. P. *J. Phys. D: Appl. Phys.* **1998**, *31*, 2886.

(24) (a) Dormann, J. L.; Tomas, A.; Nogues, M. *Phys. Status Solidi A* **1983**, *77*, 611. (b) Dormann, J. L. *Rev. Phys. Appl.* **1980**, *15*, 1113.

(25) Vucinic-Vasic, M.; Antic, B.; Blanusa, J.; Rakic, S.; Kremenovic, A.; Nikolic, A. S.; Kapor, A. *App. Phys. A* **2006**, *82*, 49–54.

(26) Visnevskii, I. I.; Alapin, B. G.; L'isak, C. V.; Skripak, V. N. *Kristalografiya* **1968**, *9*, 1079.

(27) (a) Guillot, M. Magnetic properties of Ferrites. In: *Electronic and Magnetic Properties of Metals and Ceramics*; Buschow, K. H. J., Eds.; VCH: Germany, 1994. (b) White, G. O.; Patton, C. E. *J. Magn. Magn. Mater.* **1978**, *9*, 299.

JP907559Y